

Intraseasonal variability of global land monsoon precipitation and recent change

Fei Liu (✉ liufei26@mail.sysu.edu.cn)

Sun Yat-sen university

Bin Wang

University of Hawaii at Manoa

Yu Ouyang

Shanxi Meteorological Observatory

Hui Wang

Sun Yat-sen university

Shaobo Qiao

Sun Yat-sen university

Guosen Chen

Nanjing University of Information Science & Technology

Wenjie Dong

Sun Yat-sen university

Research Article

Keywords: global monsoon, intraseasonal variability (ISV), Madden-Julian Oscillation, subseasonal prediction, High-frequency ISV, ISV trend

Posted Date: August 26th, 2021

DOI: <https://doi.org/10.21203/rs.3.rs-827388/v1>

License:   This work is licensed under a Creative Commons Attribution 4.0 International License.

[Read Full License](#)

Abstract

Accurate prediction of global land monsoon rainfall on a subseasonal (2–8 weeks) time scale has become a worldwide demand. However, the current forecasts of weekly-mean rainfall in most monsoon regions have limited skills beyond two weeks. Given that two-thirds of the world's population lives in the monsoon regions, this challenge calls for a more profound understanding of monsoon intraseasonal variability (ISVs). We show that the high-frequency (HF; 8–20 days) ISV, crucial for the Week 2 and Week 3 predictions, accounts for about 53–70% of the total (8–70 days) ISV in various land monsoon regions. The low-frequency (LF; 20–70 days) ISV has a relatively high contribution over Australia (47%), South Asia (43%), and South America (40%). The leading modes of HFISVs in Northern Hemisphere monsoons primarily originate from convectively coupled equatorial Rossby waves (Asia), mixed Rossby-gravity waves (North America), and Kelvin waves (West Africa), while in Southern Hemisphere monsoons, from mid-latitude wave trains. The Madden-Julian Oscillation (MJO) directly regulates LFISVs in the Asian-Australian monsoon while affecting the American and African monsoons by exciting Kelvin waves and mid-latitude teleconnections. During the past four decades, the HF (LF) ISVs have considerably intensified over the Asian (Asian-Australian) monsoon but weakened over the American (South American) monsoon. The presented characteristics of the ISV in each monsoon region are helpful for empirical subseasonal prediction and for identifying models' strengths and weaknesses in reproducing regional monsoon ISVs. The results suggest an urgent need to improve the simulation of convectively coupled equatorial waves and two-way interactions between regional monsoon ISVs and mid-latitude processes and between MJO and regional monsoons.

Introduction

High-quality social development with effective disaster prevention, logistics-planning, agriculture production, and decision-making requires accurate subseasonal rainfall prediction over land monsoon regions where about two-thirds of the world's population live¹. Tropical intraseasonal variabilities (ISVs) and the associated teleconnection are dominant sources of subseasonal predictability^{2–4}.

Madden-Julian Oscillation (MJO)^{5,6} is a dominant mode of tropical ISV^{2,7}. During boreal summer, MJO's eastward propagation significantly weakened, meanwhile pronounced northward and northeastward propagation prevails in the Northern Hemispheric (NH) monsoon regions^{8–13}. The MJO's impacts on regional monsoon rainfall have been extensively investigated. These include South Asian (SA)^{14–16}, East Asian (EA)^{17–19}, North American (MAM)^{20–22}, northern African (NAF)^{23–25}, Australian (AU)^{26–28}, South American (SAM)^{29–34}, and South African (SAF)^{35–37} monsoons.

Prediction of weekly-mean land monsoon rainfall at a lead of 2–8 weeks has been a major effort yet particularly challenging. The current evaluation of subseasonal prediction skill and predictability estimates has primarily focused on the leading modes of MJO or boreal summer intraseasonal oscillation^{3,38–41}. The state-of-the-art European Centre for Medium-Range Weather Forecast (ECMWF)

model can predict the leading modes of MJO up to 40 days in advance in terms of the Real-time Multivariate MJO (RMM) index^{42,43}. However, for up to four weeks, the MJO's rainfall prediction skill is confined to a narrow equatorial belt, and the rainfall prediction skills drop rapidly beyond two weeks in vast off-equatorial monsoon regions^{44,45}, as shown in Fig. 1. User community concerns with weekly rainfall prediction rather than the MJO index. What limits the subseasonal predictability of monsoon rainfall? This is the forefront challenge faced by the subseasonal prediction community.

Why does the weekly-mean monsoon rainfall prediction skill decline much faster than the MJO index skill in the prediction models? The MJO index measures the equatorial region's low-frequency (LF, 20–70 day) ISV. In most off-equatorial monsoon regions, the MJO index only accounts for a fraction of the total intraseasonal rainfall variability⁴⁶. We suspect that the Week 2 to Week 3 monsoon rainfall is mainly dominated by the high-frequency (HF, 8–20 day) ISV, not the MJO. We might not have fully recognized the importance of the HFISV in subseasonal prediction and predictability. The HFISVs in various monsoon regions have been documented. Over SA, HFISV was dominated by the westward propagating quasi-biweekly oscillation^{16,47–50}. The significant HFISV of EA precipitation was linked to preceding mid-latitude wave trains and tropical quasi-biweekly oscillation^{18,50–52}. HFISVs were also reported over NAM⁵³, NAF^{23,24,54}, AU^{27,55}, and SAM^{29,32,56–58}. However, the predictability sources of HFISV and the processes by which the equatorial disturbances and mid-latitude processes affect the HFISV in each monsoon remain elusive.

The ISVs have been investigated primarily in individual monsoon regions because each regional monsoon has an indigenous land-ocean configuration and involves different atmosphere-ocean-land interaction processes and convective and mesoscale systems. On the other hand, an across-the-board synthesis of the common and distinct features among the regional monsoons' ISVs is persuasive for an in-depth understanding, simulation, and prediction of the ISVs. The eastward-propagating planetary-scale MJO circulation system and mid-latitude disturbances may significantly regulate and coordinate the regional ISVs by changing monsoon circulations. These coordination and regional influences entail a global perspective. An overview of the ISVs of the land monsoon rainfall from a global perspective is advantageous for a deeper understanding of MJO-monsoon interaction, different characteristics and sources of regional ISV, and subseasonal prediction of regional land monsoon rainfall.

Our particular interests also include examining recent changes in regional monsoon ISVs under global warming. The seasonal-mean rainfall in the NH monsoon regions has increased considerably since 1979⁵⁹, which might have influenced the monsoon ISV. The increased rainfall over Southeast Asia, northern Australia, Southwest Africa, and Amazon were related to the increased residence times of the MJO over the Indo-Pacific Ocean and the Warm Pool expansion during the last four decades⁶⁰. The regional ISV was enhanced since 1993 over South China⁶¹. However, the changes of both HF and LF ISV intensities in most land monsoon regions remain unknown.

This study reviews and investigates the ISVs of land monsoon rainfall, including the leading modes of variability, their origins, tracks of HFISV disturbances, and recent changes in ISV intensity. The results are expected to deepen understanding of the dynamics of the monsoon ISV and improve ISV's simulation and subseasonal prediction of land monsoon rainfall.

Results

Relative importance of HF and LF ISVs in summer monsoon regions

The maximum ISV rainfall anomalies tend to anchor over the global land monsoon regions (Fig. 2a). The average ISV intensity of the global land monsoon rainfall, measured by the standard deviation of the 8-70-day filtered precipitation anomaly, is 4.6 mm day^{-1} , ranging from 3.6 mm day^{-1} (NAF monsoon) to 5.9 mm day^{-1} (AU monsoon) (Table 1). The ISV intensity is highly correlated with the corresponding seasonal-mean monsoon precipitation. The EA and SA mean monsoons have the most robust modulation on the ISV (Supplementary Fig. 1). The ISVs contribute about one-quarter to one-third to the daily precipitation variance over various land monsoon regions (Fig. 1b), ranging from 20.5% (NAF monsoon) to 32.4% (AU monsoon) (Table 1). The ISVs have relatively large contributions over Australian, South and East Asian, Mexican, and southeastern SAM monsoons but low contributions over NAF, northwestern SAF, and western SAM monsoons.

Table 1

The averaged ISV intensity for each regional land summer monsoon precipitation measured by the standard deviation shown in Fig. 1. Also shown is the fractional variance contribution of ISV to the total daily variance.

8-70-day ISV	SA	EA	NAM	NAF	AU	SAM	SAF
intensity (mm day^{-1})	5.1	4.4	4.8	3.6	5.9	4.7	4.1
contribution (%)	30.4	29.7	28.0	20.5	32.4	26.5	26.4

The regionally averaged land monsoon precipitation spectra show a significant 8-15-day HFISV peak in NH monsoons and a significant 10-20-day HFISV in the SH monsoons (Fig. 3). The precipitation spectra also show significant LF peaks in AU (30–60 days) and SA and SAM (20–40 days). No significant signal is observed beyond 70 days. Thus, we define the HF component with a time scale of 8–20 days ($\sim 2\text{--}3$ weeks) and the LF, 20–70 days ($\sim 4\text{--}9$ weeks).

The 8-20-day ISV accounts for 53–70% of the total 8-70-day ISV variance in each regional land monsoon, whereas the 20-70-day ISV accounts for 30–47% (Table 2). The EA monsoon exhibits the largest 8-20-day ISV contribution (70.2%), and the Australian monsoon has the highest 20-70-day ISV contribution (47.3%). Over AU, SA, and SAM, the HFISV contribution (53–60%) is slightly higher than LFISV (40%–47%), but over EA, NAF, NAM, and SAF, where MJO has less influence, the HFISV accounts for about 66%–70% of

the total ISV variance, dominating the ISV. The results suggest that MJO has more a significant influence on AU, SA, and SAM monsoon but less on the other four monsoon regions. The proximity of the Australian monsoon to the MJO convective activity during austral summer explains why AU monsoons have a strong LFISV component. During boreal summer, the equatorial Indian Ocean remains an MJO activity center. The prominent monsoon vertical wind shear and the northward shift of the maximum moist static energy zone favor the equatorial convective anomaly moving northward to affect SA ISV. Over the SAM, the MJO-induced mid-latitude teleconnection likely has a large amplitude^{34,62,63}, affecting SAM through the northward propagating cyclonic circulation anomalies. Due to the lower contribution of MJO to monsoon ISVs in EA, NAM, NAF, and SAF, it is interesting to find out whether the rainfall subseasonal predictability in these monsoon regions is also significantly lower than in AU, SA, and SAM.

Table 2
Fraction variance of the 8-20-day and 20-70-day ISVs to the total 8-70-day ISV for summer monsoon precipitation averaged over each monsoon region.

ISV contribution (%)	SA	EA	NAM	NAF	AU	SAM	SAF
8-20-day contribution	55.5	70.2	68.0	68.9	52.7	59.6	65.8
20-70-day contribution	44.5	29.8	32.0	31.1	47.3	40.4	34.2

The Maritime Continent is part of the monsoon region in terms of its annual reversal of the prevailing wind^{64,65}. The seasonal-mean precipitation and 8-70-day ISV intensity averaged over the Maritime Continent (100°-150°E; 10°S-5°N) are 12.5 mm day⁻¹ and 5.8 mm day⁻¹, respectively, during its wet season from November to March (Supplementary Fig. 2a). During the wet season, the Maritime Continent rainfall only shows a significant 8-20-day HFISV component (Supplementary Fig. 2b), which contributes to 58.3% of the total 8-70-day variance.

Origin and propagation of 8-20-day ISV in each monsoon region

We first identify the leading spatial pattern and activity center of the HFISV in each monsoon region. Figure 4a shows that the dominant EOF modes of the HFISVs exhibit a uniform structure in the SH monsoon and NAF monsoon regions but a north-south dipolar structure over the SA, EA, and NAM monsoon regions. The SA monsoon is characterized by wet northern India-Bangladesh and dry central India. The EA monsoon shows a contrast between a wet Southeast China and a dry Indo-China Peninsula. The NAM monsoon features a wet Venezuela and a dry Mexico. Conceivably, the North-South dipolar structures occur in the monsoon regions with a larger meridional extent, including both tropics and subtropics, so that one center in the tropical monsoon trough and the other in the subtropical convergence zone (poleward of 20° latitude). The uniform precipitation anomalies in the NAF, Australian, SAM, and the SAF monsoons are centered in Nigeria, northern Australia, Brazil, and Mozambique-Madagascar, respectively. These leading modes can explain about 9% of the 8-20-day precipitation variance, ranging from 11.4% in EA to 7.2% in SAF. Note that the second EOF modes have a comparable

fractional variance to the first one (Supplementary Table 1). Together, they depict a propagating mode so that the two leading modes explain about 15% of the variance.

Where are the peak phases of the leading 8-20-day ISV modes originated? Fig. 5 presents sequential maps of the regressed OLR and wind anomalies that trace their origins and propagation pathways. On Day 0, the regressed OLR anomalies are consistent with the precipitation anomalies associated with the leading 8-20-day ISV pattern shown in Fig. 4a.

Over SA (Fig. 5a), the low-level anticyclonic anomaly that couples with the suppressed convection emerges over the Philippine Sea around 135°E on Day - 8. It then moves westward along 10-20°N, finally forming a suppressed rain band stretching from central India to the Bay of Bengal on Day 0. The southwesterly anomalies to the north of the anticyclonic circulation strengthen moisture transport and convergence, leading to enhanced convection over northern India-Bangladesh. The zonally elongated anticyclone stretches approximately 50° in longitude, and the westward phase speed is about 7.2 m s⁻¹. This feature is consistent with previous findings^{16,47,48}. An apparent upper-tropospheric wave train also moves westward along 40°N from eastern China to the Iranian Plateau against the background westerlies (Supplementary Fig. 3a), suggesting that the upper-level circulation anomalies are likely a response to the convective heating rather than an extratropical forcing. This strong upper-tropospheric wave train indicates that the SA precipitation can significantly modulates the mid-latitude circumglobal teleconnection⁶⁶, “silk road” teleconnection^{67,68}, and the Tibetan Plateau⁶⁹ on the HF intraseasonal time scale.

In EA (Fig. 5b), an anticyclonic anomaly emerges from the western equatorial Pacific around 140°E on Day - 8; it propagates northwestward and is accompanied by suppressed convection, reaching the South China Sea and Indo-China Peninsula on Day 0. The westward phase speed is about 3.5 m s⁻¹, consistent with previous results, e. g., Chen and Chen⁷⁰. This northwestward propagation pathway is similar to the 8-10-day disturbances documented by Lau and Lau⁷¹. In theory, moist Rossby waves can emanate from the equatorial convective anomalies when the equatorial intraseasonal convective anomalies decay, passing through the western Pacific. They then move northwestward under the influence of background monsoon easterly vertical wind shear Fig. 4 in Wang and Xie⁹. Note that from Day - 2 to Day 0 the convection over Southeast China is enhanced by the convergence of southwesterly wind anomalies to its northwest, forming the dipolar structure. In addition to the tropical origin mentioned above, a lower-tropospheric cyclonic wind anomaly emerges to the east of Lake Baikal and propagates southeastward (Fig. 5b). The southwest part of this cyclonic anomaly triggers convection over eastern China on Day - 2, and the convection peaks on Day 0. Meanwhile, the major body of the cyclonic anomaly propagates into the North Pacific. The evidence here seems to confirm previous findings concerning the influence of the mid-latitude wave trains on the quasi-biweekly variability of EA summer monsoon^{51,52,72}.

Over the NAM and NAF monsoon regions, the OLR anomalies are relatively weak (Figs. 5c and 5d). However, their precipitation anomalies are not (Fig. 4a), suggesting that shallower convection may prevail

over these two regions, a feature similar to the corresponding seasonal-mean precipitation^{73–75}. For the NAM monsoon, an incipient low-level cross-equatorial southerly anomaly emerges in the central equatorial Atlantic on Day – 6, which couples with enhanced convection and propagates westward, reaching a peak over Venezuela on Day 0 (Fig. 5c). The coupling of the enhanced convection with an upper-level cross-equatorial northerly anomaly is more obvious (Supplementary Fig. 3c). Meanwhile, a suppressed convection propagates from Venezuela on Day – 8 to the Gulf of Mexico on Day 0, initially coupling with a cross-equatorial northerly and later with an anticyclonic anomaly. Along the equatorial Atlantic, the convective anomaly coupled with the cross-equatorial flow looks like a mixed Rossby-gravity wave⁷⁶. We suggest that the 8-20-day ISV in the NAM region originates from an equatorial mixed Rossby-gravity wave and gradually transforms to a convectively coupled Rossby wave. No significant mid-latitude wave train is observed (Supplementary Fig. 3c).

The HFISV over NAF has a weak convective anomaly, which appears to be excited by upper-level divergence associated with a fast eastward-propagating equatorial Kelvin wave (Fig. 5d). The upper-level Kelvin wave easterly anomalies emerge over the eastern equatorial Pacific around 120°W on Day – 6, propagate eastward, and reach the eastern Atlantic around 10°W on Day 0, with a phase speed of about 24 m s⁻¹. The convection over NAF is then enhanced by the divergent flows associated with the easterly anomalies. The low-tropospheric westerly anomalies related to this Kelvin wave are relatively weak before reaching the Atlantic (Supplementary Fig. 3d).

Unlike the NH, the SH HFISVs in all three monsoons are associated with significant mid-latitude wave trains in the lower (Fig. 6) and upper troposphere (Supplementary Fig. 4). Over Australia, the burst of monsoon convection on Day – 2 is triggered by a low-pressure trough associated with a cyclonic anomaly over Central Australia. This cyclonic anomaly was originated in the southeastern Indian Ocean on Day – 8 and propagated eastward to Southeast Australia on Day 0 (Fig. 6a). In SAM, a cyclonic anomaly emerges over the South Atlantic along 50°S on Day – 8, which propagates northward first, and then turns westward on Day – 6, triggering the convection over SAM on Day – 2 (Fig. 6b). The convection anomaly couples with the cyclonic anomaly and matures on Day 0. The northward and westward propagations were also associated with the sub-monthly oscillation of the Brazil rainfall or South Atlantic Convergence Zone^{57,58,77}. The role of mid-latitude wave trains on the ISV is also observed for the SAF monsoon (Fig. 6c). A mid-latitude low-level cyclonic anomaly propagates from the area over the Southeast Atlantic on Day – 8 to the region over the southwestern Indian Ocean on Day 0. The cyclonic anomaly triggers the convection in Zimbabwe on Day – 4 and then propagates northeastward and matures near Madagascar on Day 0. The corresponding propagations of the upper-tropospheric cyclonic anomalies for the three SH monsoons illustrate the mid-latitude wave trains' equivalent barotropic structures (Figs. 6 and S4). However, once coupled with convection in the monsoon region, the barotropic structure transforms to a baroclinic structure.

Figure 4a presents a schematic diagram to summarize the HFISVs' origins and pathways. The ISVs in Asian monsoons are related to the preceding tropical quasi-biweekly oscillation originated from the

western equatorial Pacific. The EA monsoon is additionally associated with southward-propagating mid-latitude wave trains. The HFISVs over NAM and NAF are triggered by the convectively coupled mixed Rossby-gravity and Kelvin waves, respectively. Besides, the westward propagation of HFISV from Venezuela to Mexico is accompanied by a transition from a mixed Rossby-gravity wave to an equatorial Rossby wave. All three SH monsoons are related to preceding mid-latitude wave trains in the SH.

The different origins of HFISVs are likely determined by monsoon locations and background circulations, as discussed over EA by Liu, et al. ⁵². The SH monsoon HFISVs are triggered by the mid-latitude wave trains because of their proximity to the westerly jet stream (Figs. 4a and S5). Likewise, the EA monsoon is also exposed to the mid-latitude wave train's impact. On the other hand, NAM and NAF are close to the equator. Thus, their HFISVs originate from the convectively coupled equatorial waves.

MJO Coordination of 20-70-day ISV in each monsoon region

The leading modes of LF (20-70-day) ISVs have similar spatial patterns as the corresponding HF (8-20-day) ISVs for each monsoon (Fig. 4). Nevertheless, minor differences exist. In SA, the Central Indian precipitation anomaly is stronger than that in northern India-Bangladesh (Fig. 4b). In NAM, the Mexican precipitation anomaly is stronger than the Venezuela anomaly. The similarity between the spatial patterns of the HF and LF ISVs implies that the mean regional monsoon circulation might have similar controls on the HF and LF ISVs. The HF and LF ISVs may also interact with each other. In the SA, AU, and SAM regions, where the LFISVs have significant contributions to the total ISV (Table 2), the first EOF mode explains 22.6%, 18.5%, and 17.0% of the total 20-70-day variance, more than double the fractional variance of the corresponding second modes (Supplementary Table 1). It suggests that the monsoon responses to the MJO over SA, AU, and SAM seem to be geographically-locked amplification rather than a propagating mode. Conversely, in other monsoons where the HF dominates the ISV, the first two modes of LFISVs have comparable fractional variances, indicating a propagating mode.

As summarized in Fig. 4b, the 20-70-day ISV in Central India is related to the northward propagation of the boreal summer ISO from the equatorial Indian Ocean. The Southeast China precipitation is enhanced by the southwesterly wind anomaly of the western North Pacific suppressed ISO that originates from the Indian Ocean, consistent with previous works^{8,48,78}. In SH, the Australian monsoon 20-70-day ISV is dominantly affected by the MJO convection over the Arafura Sea, as demonstrated by^{28,79}. The MJO modulates other monsoon regions primarily by exciting convectively coupled Kelvin waves. Significant preceding MJO convection anomalies are observed over the Warm Pool region. The MJO-excited Kelvin waves, represented by upper-level easterly anomalies, propagate eastward along the equator and enhance the convection over the Gulf of Mexico (Supplementary Fig. 6a), Nigeria (Supplementary Fig. 6b), Brazil (Supplementary Fig. 6c), and Zambia-Madagascar (Supplementary Fig. 6d). The influential Kelvin waves for SH monsoons are weaker than NH monsoons (Supplementary Fig. 6), indicating a stronger mid-latitude teleconnection of MJO due to strong SH westerly jet (Supplementary Fig. 5).

Significant preceding mid-latitude wave trains are observed in SAM. The wave train associated with SAM originated to the east of Australia, tied to the MJO convection anomaly over the tropical western Pacific

(Supplementary Fig. 6c). This Indo-Pacific MJO's impact on the SAM through the mid-latitude teleconnection has also been observed by Roundy⁶³ and Grimm³⁴. Since the group speed of the teleconnection is quite fast, and the MJO's signal can reach the America in about one week^{80,81} so that the SAM only lags the Indo-Pacific MJO by 10 days.

In summary (Fig. 4b), the 20-70-day ISVs of the Asian-Australian monsoon are directly affected by the MJO propagation. The Indo-Pacific MJO influences the American and African monsoons through its eastward-propagating Kelvin component and also has robust impacts on the SAM through its mid-latitude teleconnection in the SH.

Figure 7 summarizes the relationship between the MJO peak wet phase over the central equatorial Indian Ocean (or dry phase over the tropical western Pacific) and each region's leading mode of 20-70-day ISV. All these correlations are significant, except for the African monsoons. MJO peak phase has the strongest linkages with AU, SA, and SAM. The MJO peak wet phase over the Indian Ocean leads the AU wet phase by 14 days with the highest $r=0.3$ ($p<0.01$) and the SA wet phase by 12 days with $r=0.26$ ($p<0.01$), respectively. The MJO dry phase over the western equatorial Pacific, which concurs with the equatorial Indian Ocean wet phase, leads the SAM dry phase by ten days with $r=0.25$ ($p<0.01$). The high correlations in these regions are consistent with their higher fractional variance of the ISV to daily variance (Fig. 2b) and the higher contribution of the LFISV to the total ISV (Table 2). In addition, the enhanced MJO convection over the central equatorial Indian Ocean tends to lead the wet Southeast Asia and dry South China by 22 days. The dry anomaly over the tropical western Pacific leads the dry phase by 15 days over Mexico and by ten days over Brazil. These lead-lag correlations can be potentially used for the subseasonal prediction of each regional monsoon.

Recent trends

We observe a significant ($p<0.01$) increasing trend in the amplitude of HFISVs over Southeast China and northern India-Bangladesh during the past four decades (Fig. 8). The largest increasing trend (about 35% per four decades) is over northern India-Bangladesh. In contrast, decreasing trends occur over South America, including significantly ($p<0.05$) weakening over Venezuela (9%) and Brazil (9%). The LFISVs are enhanced over Central Indian, Southeast China, and Australia with a trend of 16% ($p<0.1$), 22% ($p<0.01$), and 15% ($p<0.1$), respectively. The decreasing LFISV is found over Brazil (13%, $p<0.01$).

The changes of ISV intensity follow those of seasonal-mean precipitation (Fig. 8). The mean precipitation exhibits a significant increasing trend over Southeast China, Central India, northern India-Bangladesh, and Australia. Meanwhile, a significant decreasing trend appears over Venezuela and Brazil, resulting in a significant reduction in ISV intensity. The increased mean precipitation in Asian monsoons during the last four decades is mainly due to the negative phase of the Inter-decadal Pacific Oscillation and the warm phase of the Atlantic Multi-decadal Oscillation, augmented by increased greenhouse gas (GHG) emission^{59,82}. The year-to-year variations of the ISV intensity over different land monsoons are also significantly correlated to the variations of corresponding mean precipitation (Supplementary Fig. 7). All

these results indicate that the intensity change of individual monsoon ISVs is determined by local mean-state change.

Discussion

Monsoon regions host the maximum intraseasonal rainfall anomalies during local summer monsoon seasons over the global land areas (Fig. 2a). The averaged ISV intensity (standard deviation) is about half of the seasonal-mean precipitation (9.3 mm day^{-1}) and about one-quarter to one-third of the daily precipitation variance (Table 1). The ISV intensity closely follows the corresponding seasonal-mean precipitation intensity, and EA and SA mean monsoons have the most robust modulation on the ISV (Supplementary Fig. 1). The area-averaged land monsoon rainfall spectra show a significant 8-20-day (HF) ISV peak in all eight regional monsoons (including the maritime continent) and significant 20-70-day (LF) peaks in Australia, SA, and SAM monsoons (Fig. 3). The HFISV accounts for about 53–70% of the total ISV in the land monsoon regions, dominating the subseasonal variability of monsoon rainfall (Table 2). The LFISV has a relatively large fractional contribution to the total ISV over Australian (47%), SA (45%), and SAM (40%) monsoons.

The wet phase of HFISV in each monsoon region is preceded by diverse precursors and propagation routes (Figs. 4a, 5, and 6). The Asian monsoon's HFISVs are primarily related to the westward-propagating quasi-biweekly oscillation disturbances originated from the western equatorial Pacific. The NAM and NAF monsoons' HFISVs find their preceding signals from convectively coupled mixed Rossby-gravity waves and equatorial Kelvin waves, respectively. In contrast, all three SH monsoons are initiated by mid-latitude wave trains. These divergent origins and propagations of HFISVs are primarily determined by the geographic locations of the monsoons and their associated background circulations.

The MJO directly affects the 20-70-day LFISVs of the Australian monsoon during its eastward journey in boreal winter and Asian summer monsoon by northward and northeastward propagation under the influence of the background monsoon circulation (Fig. 4b). The powerful monsoon flows shift the maximum moist static energy zone northward and provide easterly vertical shear, favoring convectively coupled ISV moving northward. On the other hand, the MJO influences American and African monsoons primarily through its associated Kelvin wave component (Fig. 4b). Besides, the MJO has a substantial impact on the SAM through its mid-latitude teleconnection in the SH.

The HFISV activity has significantly intensified over the past 40 years in Southeast China and northern India-Bangladesh. Similarly, the LFISV displays a significant increasing trend over Central India, Southeast China, and northern Australia (Fig. 8). The top increasing trend reached 35% over northern India-Bangladesh. On the other hand, a significant decreasing trend is observed over Venezuela for the HFISV and over Brazil for both HF and LF ISVs. These ISV intensity changes follow the corresponding seasonal-mean precipitation changes, suggesting a local monsoon mean-state control over ISV changes. Observed changes in the mean monsoon rainfall vary by region with significant decadal variations. The NH land monsoon rainfall as a whole has increased since 1980 due to the competing influences of

internal climate variability and radiative forcing from GHGs and aerosol forcing; however, it remains a challenge to quantify their relative contributions⁸³.

The results suggest that better understanding and modeling HFISV is critical to subseasonal-to-seasonal prediction as it accounts for 53–70% of the total ISV. There is an urgent need to investigate HFISV more extensively as it may be crucial for improving the Week 2 and Week 3 monsoon rainfall forecast. The close connections between the NH monsoon HFISVs and the convectively coupled equatorial waves suggest the importance of faithfully simulating convectively coupled equatorial waves in the forecast models. Given the close linkage between the HFISV and midlatitude wave trains in the SH and EA monsoons, untangling and quantifying the roles of mid-latitude and off-equatorial processes in monsoon rainfall ISV should be a priority. The characteristics of the HFISV illustrated in each monsoon region (Figs. 4a, 5, and 6) could help identify models' strengths and weaknesses in reproducing regional characteristics of the ISVs. The lead-lag relationships between the MJO and each regional monsoon (Fig. 7) provide potential useful statistics for empirical subseasonal prediction and for gauging the models' fidelity in reproducing the MJO-monsoon LFISV relationship. The strong ISV of global land monsoon rainfall also calls for investigation of two-way interaction between regional monsoon and MJO and between regional monsoon ISV and mid-latitude and off-equatorial processes.

Methods

The data used in this study include 1) daily Climate Prediction Center global precipitation data with a high resolution of $0.5^\circ \times 0.5^\circ$, provided by the National Oceanic and Atmospheric Administration (NOAA)^{84,85}; 2) daily outgoing longwave radiation (OLR) data with a resolution of $2.5^\circ \times 2.5^\circ$ from the NOAA⁸⁶, as a proxy for large-scale organized deep convection in the tropics^{11,12,42}; 3) daily winds of the Reanalysis II data from the National Centers for Environmental Prediction⁸⁷; and 4) daily RMM index of Wheeler and Hendon⁴² from the Australian Bureau of Meteorology. The change of MJO signal over the central equatorial Indian Ocean can be represented by the negative RMM2 index⁴².

The study period covers 40 years, from 1979 to 2018. The summer season denotes May to September for the NH and November to March for the Southern Hemisphere (SH). Here, we focus on land monsoon precipitation. The global monsoon domains are defined by the regions where the summer-minus-winter precipitation exceeds 300 mm, and summer precipitation exceeds 55% of the annual total^{88,89}.

We applied the Lanczos bandpass filter⁹⁰ to daily anomalies to extract the HF and LF signals. To calculate fractional variance contribution, we display power spectra of precipitation time series in the area-conserving format, i.e., the logarithm of frequency versus the product of the power and frequency, in which variance is proportional to the area^{42,91}. The contribution of HF and LF ISVs to the total daily precipitation variance can be determined by the area ratio of each ISV band versus the total area.

We performed the empirical orthogonal function (EOF) analysis on the filtered data to reveal the dominant patterns of the HF and LF ISVs during the summer monsoon season. Each principal

component (PC) is normalized by its standard deviation, and the EOF pattern is scaled by multiplying this standard deviation. The Theil-Sen trend estimation method is applied to the linear trend, significantly more accurate than simple linear regression for skew and heteroscedastic data^{92,93}. The statistical significance levels are tested using the Mann-Kendall rank statistics⁹⁴. Lead-lag regression maps are used to detect potential predictability sources of the ISV patterns for each monsoon region. We tested statistical significance based on the two-tailed Student's *t*-test with the effective degree of freedom for the filtered data⁹⁵.

DATA AVAILABILITY

The data that support the findings of this study are openly available and they can be found in the respective references.

Declarations

DATA AVAILABILITY

The data that support the findings of this study are openly available and they can be found in the respective references.

ACKNOWLEDGEMENTS

This work was supported by the Natural Science Foundation of China (41975107). BW acknowledges the support from the National Science Foundation (award #2025057).

AUTHOR CONTRIBUTIONS

F.L. and B.W. conceived the idea and proposed this study. Y.O. conducted the data analyses. All the authors discussed the concepts. The manuscript was drafted by F.L. and B.W. and edited by all authors.

COMPETING INTERESTS

The authors declare no competing interests.

References

1. Webster, P. J. & Hoyos, C. D. Prediction of monsoon rainfall and river discharge on 15-30-day time scales. *Bull. Amer. Meteor. Soc.* **85**, 1745-1765 (2004).
2. Lau, W. K. M. & Waliser, D. E. *Intraseasonal variability of the atmosphere–ocean–climate system*. (Springer Berlin Heidelberg, 2011).
3. Vitart, F. et al. The Subseasonal to Seasonal (S2S) Prediction Project Database. *Bull. Amer. Meteor. Soc.* **98**, 163-173 (2017).

4. Stan, C. et al. Review of Tropical-Extratropical Teleconnections on Intraseasonal Time Scales. *Rev. Geophys.* **55**, 902-937 (2017).
5. Madden, R. A. & Julian, P. R. Detection of a 40-50 Day Oscillation in the Zonal Wind in the Tropical Pacific. *J. Atmos. Sci.* **28**, 702-708 (1971).
6. Madden, R. A. & Julian, P. R. Description of Global-Scale Circulation Cells in the Tropics with a 40-50 Day Period. *J. Atmos. Sci.* **29**, 1109-1123 (1972).
7. Zhang, C. Madden-Julian Oscillation. *Rev. Geophys.* **43**, 453-468 (2005).
8. Wang, B. & Rui, H. Synoptic climatology of transient tropical intraseasonal convection anomalies: 1975–1985. *Meteorol. Atmos. Phys.* **44**, 43-61 (1990).
9. Wang, B. & Xie, X. A Model for the Boreal Summer Intraseasonal Oscillation. *J. Atmos. Sci.* **54**, 72-86 (1997).
10. Webster, P. J. et al. Monsoons: Processes, predictability, and the prospects for prediction. *J. Geophys. Res.-Atmos.* **1031**, 14451-14510 (1998).
11. Kikuchi, K., Wang, B. & Kajikawa, Y. Bimodal representation of the tropical intraseasonal oscillation. *Clim. Dyn.* **38**, 1989-2000 (2012).
12. Lee, J.-Y. et al. Real-time multivariate indices for the boreal summer intraseasonal oscillation over the Asian summer monsoon region. *Clim. Dyn.* **40**, 493-509 (2013).
13. Hendon, H. H. & Salby, M. L. The Life Cycle of the Madden–Julian Oscillation. *J. Atmos. Sci.* **51**, 2225-2237 (1994).
14. Yasunari, T. Structure of an Indian Summer Monsoon System with around 40-Day Period. *J. Meteor. Soc. Japan* **59**, 336-354 (1981).
15. Hartmann, D. & Michelsen, M. Intraseasonal Periodicities in Indian Rainfall. *J. Atmos. Sci.* **46**, 2838-2862 (1989).
16. Annamalai, H. & Slingo, J. M. Active/break cycles: diagnosis of the intraseasonal variability of the Asian Summer Monsoon. *Clim. Dyn.* **18**, 85-102 (2001).
17. Chen, L. X., Zhu, C. W., Wang, W. & Zhang, P. Q. Analysis of the characteristics of 30-60 day low-frequency oscillation over Asia during 1998 SCSMEX. *Adv. Atmos. Sci.* **18**, 623-638 (2001).
18. Liang, P. & Ding, Y. Climatologic characteristics of the intraseasonal oscillation of East Asian meiyu. *Acta Meteorologica Sinica* **70**, 418-435 (2012).

19. Hsu, P.-C., Lee, J.-Y. & Ha, K.-J. Influence of boreal summer intraseasonal oscillation on rainfall extremes in southern China. *Int. J. Climatol.* **36**, 1403-1412 (2016).
20. Higgins, R. W. & Shi, W. Intercomparison of the principal modes of interannual and intraseasonal variability of the North American Monsoon System. *J. Clim.* **14**, 403-417 (2001).
21. Barlow, M. & Salstein, D. Summertime influence of the Madden-Julian Oscillation on daily rainfall over Mexico and Central America. *Geophys. Res. Lett.* **33** (2006).
22. Perdigon-Morales, J., Romero-Centeno, R., Barrett, B. S. & Ordonez, P. Intraseasonal Variability of Summer Precipitation in Mexico: MJO Influence on the Midsummer Drought. *J. Clim.* **32**, 2313-2327 (2019).
23. Sultan, B., Janicot, S. & Diedhiou, A. The West African monsoon dynamics. Part I: Documentation of intraseasonal variability. *J. Clim.* **16**, 3389-3406 (2003).
24. Maloney, E. D. & Shaman, J. Intraseasonal variability of the West African monsoon and Atlantic ITCZ. *J. Clim.* **21**, 2898-2918 (2008).
25. Janicot, S., Mounier, F., Gervois, S., Sultan, B. & Kiladis, G. N. The Dynamics of the West African Monsoon. Part V: The Detection and Role of the Dominant Modes of Convectively Coupled Equatorial Rossby Waves. *J. Clim.* **23**, 4005-4024 (2010).
26. Hendon, H. H. & Liebmann, B. The intraseasonal (30-50 day) oscillation of the Australian summer monsoon. *J. Atmos. Sci.* **47**, 2909-2923 (1990).
27. Wheeler, M. C. & McBride, J. L. in *Intraseasonal Variability in the Atmosphere-Ocean Climate System* (eds William K. M. Lau & Duane E. Waliser) 125-173 (Springer Berlin Heidelberg, 2005).
28. Wheeler, M., Hendon, H., Cleland, S., Meinke, H. & Donald, A. Impacts of the Madden-Julian Oscillation on Australian Rainfall and Circulation. *J. Clim.* **22** (2009).
29. Nogués-Paegle, J., Byerle, L. A. & Mo, K. C. Intraseasonal modulation of South American summer precipitation. *Mon. Wea. Rev.* **128**, 837-850 (2000).
30. Liebmann, B., Kiladis, G. N., Vera, C. S., Saulo, A. C. & Carvalho, L. M. V. Subseasonal variations of rainfall in South America in the vicinity of the low-level jet east of the Andes and comparison to those in the South Atlantic convergence zone. *J. Clim.* **17**, 3829-3842 (2004).
31. Alvarez, M. S., Vera, C. S., Kiladis, G. N. & Liebmann, B. Influence of the Madden Julian Oscillation on precipitation and surface air temperature in South America. *Clim. Dyn.* **46**, 245-262 (2016).
32. Vera, C. S., Alvarez, M. S., Gonzalez, P. L. M., Liebmann, B. & Kiladis, G. N. Seasonal cycle of precipitation variability in South America on intraseasonal timescales. *Clim. Dyn.* **51**, 1991-2001 (2018).

33. Carvalho, L. M. V., Jones, C. & Liebmann, B. The South Atlantic convergence zone: Intensity, form, persistence, and relationships with intraseasonal to interannual activity and extreme rainfall. *J. Clim.* **17**, 88-108 (2004).
34. Grimm, A. M. Madden-Julian Oscillation impacts on South American summer monsoon season: precipitation anomalies, extreme events, teleconnections, and role in the MJO cycle. *Clim. Dyn.* **53**, 907-932 (2019).
35. Pohl, B. & Camberlin, P. Influence of the Madden–Julian Oscillation on East African rainfall. I: Intraseasonal variability and regional dependency. *Q. J. R. Meteorol. Soc.* **132**, 2521-2539 (2006).
36. Berhane, F. & Zaitchik, B. Modulation of Daily Precipitation over East Africa by the Madden-Julian Oscillation. *J. Clim.* **27**, 6016-6034 (2014).
37. Camberlin, P., Gitau, W., Kiladis, G. N., Bosire, E. & Pohl, B. Intraseasonal to Interannual Modulation of Diurnal Precipitation Distribution Over Eastern Africa. *J. Geophys. Res.-Atmos.* **124**, 11863-11886 (2019).
38. Martin, Z. et al. The influence of the quasi-biennial oscillation on the Madden–Julian oscillation. *Nat. Rev. Earth Environ.* (2021).
39. Lee, S.-S., Wang, B., Waliser, D. E., Neena, J. M. & Lee, J.-Y. Predictability and prediction skill of the boreal summer intraseasonal oscillation in the Intraseasonal Variability Hindcast Experiment. *Clim. Dyn.* **45**, 2123-2135 (2015).
40. Neena, J. M., Lee, J. Y., Waliser, D. & Wang, B. Predictability of the Madden-Julian Oscillation in the Intraseasonal Variability Hindcast Experiment (ISVHE). *J. Clim.* **27**, 4531-4543 (2014).
41. Meehl, G. A. et al. Initialized Earth System prediction from subseasonal to decadal timescales. *Nat. Rev. Earth Environ.* **2**, 340-357 (2021).
42. Wheeler, M. C. & Hendon, H. H. An all-season real-time multivariate MJO index : Development of an index for monitoring and prediction. *Mon. Wea. Rev.* **132**, 1917-1932 (2004).
43. Lim, Y., Son, S. W. & Kim, D. MJO Prediction Skill of the Subseasonal-to-Seasonal Prediction Models. *J. Clim.* **31**, 4075–4094 (2018).
44. Li, S. & Robertson, A. Evaluation of Sub-monthly Precipitation Forecast Skill from Global Ensemble Prediction Systems. *Mon. Wea. Rev.* **143**, 2871–2889 (2015).
45. de Andrade, F. M., Coelho, C. A. S. & Cavalcanti, I. F. A. Global precipitation hindcast quality assessment of the Subseasonal to Seasonal (S2S) prediction project models. *Clim. Dyn.* **52**, 5451-5475 (2019).

46. Lee, S. S. & Wang, B. Regional boreal summer intraseasonal oscillation over Indian Ocean and Western Pacific: comparison and predictability study. *Clim. Dyn.* **46**, 2213-2229 (2016).
47. Krishnamurti, T. & Bhalme, H. Oscillations of a Monsoon System. Part I. Observational Aspects. *J. Atmos. Sci.* **33**, 1937-1954 (1976).
48. Yasunari, T. Cloudiness Fluctuations Associated with the Northern Hemisphere Summer Monsoon. *J. Meteor. Soc. Japan* **57**, 227-242 (1979).
49. Kikuchi, K. & Wang, B. Global Perspective of the Quasi-Biweekly Oscillation. *J. Clim.* **22**, 1340-1359 (2009).
50. Qian, Y., Hsu, P.-C. & Kazuyoshi, K. New real-time indices for the quasi-biweekly oscillation over the Asian summer monsoon region. *Clim. Dyn.* **53**, 2603-2624 (2019).
51. Yang, J., Wang, B. & Bao, Q. Biweekly and 21–30-Day Variations of the Subtropical Summer Monsoon Rainfall over the Lower Reach of the Yangtze River Basin. *J. Clim.* **23**, 1146-1159 (2010).
52. Liu, F. et al. Seasonal evolution of the intraseasonal variability of China summer precipitation. *Clim. Dyn.* **54**, 4641-4655 (2020).
53. Mo, K. C. Intraseasonal modulation of summer precipitation over North America. *Mon. Wea. Rev.* **128**, 1490-1505 (2000).
54. Mounier, F., Janicot, S. & Kiladis, G. N. The west African monsoon dynamics. Part III: The quasi-biweekly zonal dipole. *J. Clim.* **21**, 1911-1928 (2008).
55. Wheeler, M. C. & McBride, J. L. in *Intraseasonal Variability in the Atmosphere-Ocean Climate System* (eds William K. M. Lau & Duane E. Waliser) 147-197 (Springer Berlin Heidelberg, 2011).
56. Gonzalez, P. L. M. & Vera, C. S. Summer precipitation variability over South America on long and short intraseasonal timescales. *Clim. Dyn.* **43**, 1993-2007 (2014).
57. Liebmann, B., Kiladis, G. N., Marengo, J., Ambrizzi, T. & Glick, J. D. Submonthly Convective Variability over South America and the South Atlantic Convergence Zone. *J. Clim.* **12**, 1877-1891 (1999).
58. Nogués-Paegle, J. & Mo, K. C. Alternating Wet and Dry Conditions over South America during Summer. *Mon. Wea. Rev.* **125**, 279-291 (1997).
59. Wang, B. et al. Northern Hemisphere summer monsoon intensified by mega-El Niño/southern oscillation and Atlantic multidecadal oscillation. *Proc. Natl. Acad. Sci. USA* **110**, 5347-5352 (2013).
60. Roxy, M. K. et al. Twofold expansion of the Indo-Pacific warm pool warps the MJO life cycle. *Nature* **575**, 647-651 (2019).

61. Cheng, Y., Wang, L. & Li, T. Causes of Interdecadal Increase in the Intraseasonal Rainfall Variability over Southern China around the Early 1990s. *J. Clim.* **33**, 1-47 (2020).
62. Mo, K. C., Jones, C. & Paegle, J. N. in *Intraseasonal Variability in the Atmosphere-Ocean Climate System* 111-145 (Springer Berlin Heidelberg, 2012).
63. Roundy, P. E. in *Intraseasonal Variability in the Atmosphere-Ocean Climate System* 497-512 (Springer Berlin Heidelberg, 2012).
64. Chang, C. P., Wang, Z., McBride, J. & Liu, C.-H. Annual Cycle of Southeast Asia - Maritime Continent Rainfall and the Asymmetric Monsoon Transition. *J. Clim.* **18**, 287-301 (2005).
65. Ramage, C. S. *Monsoon Meteorology*. 296 (New York, NY: Academic 1971).
66. Ding, Q. & Wang, B. Circumglobal Teleconnection in the Northern Hemisphere Summer. *J. Clim.* **18**, 3483-3505 (2005).
67. Enomoto, T., Hoskins, B. J. & Matsuda, Y. The formation mechanism of the Bonin high in August. *Q. J. R. Meteorol. Soc.* **129**, 157-178 (2003).
68. Lu, R., Ryu, C.-S. & Dong, B. Associations between the Western North Pacific Monsoon and the South China Sea Monsoon. *Adv. Atmos. Sci.* **19**, 12-24 (2002).
69. Yang, J. et al. Characterizing two types of transient intraseasonal oscillations in the Eastern Tibetan Plateau summer rainfall. *Clim. Dyn.* **48**, 1749-1768 (2017).
70. Chen, T.-C. & Chen, J.-M. The Intraseasonal Oscillation of the Lower-Tropospheric Circulation over the Western Pacific during the 1979 Northern Summer. *J. Meteor. Soc. Japan* **71**, 205-220 (1993).
71. Lau, K.-H. & Lau, N.-C. Observed structure and propagation characteristics of tropical summertime synoptic scale disturbances. *Mon. Wea. Rev.* **118**, 1888-1913 (1990).
72. Gao, M. et al. How are heat waves over Yangtze River valley associated with atmospheric quasi-biweekly oscillation? *Clim. Dyn.* **51**, 4421-4437 (2018).
73. Zhang, C., Nolan, D. S., Thorncroft, C. D. & Nguyen, H. Shallow meridional circulations in the tropical atmosphere. *J. Clim.* **21**, 3453-3470 (2008).
74. Nie, J., Boos, W. R. & Kuang, Z. Observational Evaluation of a Convective Quasi-Equilibrium View of Monsoons. *J. Clim.* **23**, 4416-4428 (2010).
75. Waliser, D. E., Graham, N. E. & Gautier, C. Comparison of the Highly Reflective Cloud and Outgoing Longwave Radiation Datasets for Use in Estimating Tropical Deep Convection. *J. Clim.* **6**, 331-353 (1993).

76. Kiladis, G. N., Wheeler, M. C., Haertel, P. T., Straub, K. H. & Roundy, P. E. Convectively coupled equatorial waves. *Rev. Geophys.* **47** (2009).
77. Kousky, V. E. Frontal Influences on Northeast Brazil. *Mon. Wea. Rev.* **107**, 1140-1153 (1979).
78. Kemball-cook, S. & Wang, B. Equatorial Waves and Air-Sea Interaction in the Boreal Summer Intraseasonal Oscillation. *J. Clim.* **14**, 2923-2942 (2001).
79. Moise, A., Smith, I., Brown, J., Colman, R. & Narsey, S. Observed and projected intra-seasonal variability of Australian monsoon rainfall. *Int. J. Climatol.* **40**, 2310-2327 (2019).
80. Cassou, C. Intraseasonal interaction between the Madden-Julian Oscillation and the North Atlantic Oscillation. *Nature* **455**, 523-527 (2008).
81. Moon, J. Y., Wang, B. & Ha, K. J. ENSO regulation of MJO teleconnection. *Clim. Dyn.* **37**, 1133-1149 (2011).
82. Wang, B. et al. Toward Predicting Changes in the Land Monsoon Rainfall a Decade in Advance. *J. Clim.* **31**, 2699-2714 (2018).
83. Wang, B. et al. Monsoons Climate Change Assessment. *Bull. Amer. Meteor. Soc.* **102**, E1-E19 (2021).
84. Xie, P. et al. A Gauge-Based Analysis of Daily Precipitation over East Asia. *J. Hydrometeorol.* **8**, 607-626 (2007).
85. Chen, M. et al. Assessing objective techniques for gauge-based analyses of global daily precipitation. *J. Geophys. Res.-Atmos.* **113** (2008).
86. Liebmann, B. & Smith, C. Description of a complete (interpolated) outgoing longwave radiation dataset. *Bull. Amer. Meteor. Soc.* **77**, 1275-1277 (1996).
87. Kanamitsu, M. et al. NCEP dynamical seasonal forecast system 2000. *Bull. Amer. Meteor. Soc.* **83**, 1019–1038 (2002).
88. Lee, J.-Y. & Wang, B. Future change of global monsoon in the CMIP5. *Clim. Dyn.* **42**, 101-119 (2014).
89. Wang, B. & Ding, Q. Global monsoon: Dominant mode of annual variation in the tropics. *Dyn. Atmos. Oceans* **44**, 165-183 (2008).
90. Duchon, C. Lanczos Filtering in One and Two Dimensions. *J. Appl. Meteorol.* **18**, 1016-1022 (1979).

91. Zangvil, A. On the Presentation and Interpretation of Spectra of Large-Scale Disturbances. *Mon. Wea. Rev.* **105**, 1469–1472 (1977).
92. Wilcox, R. R. Simulation results on extensions of the theil-sen regression estimator. *Commun. Stat.-Simul. Comput.* **27**, 1117-1126 (1998).
93. Akritas, M. G., Murphy, S. A. & Lavalley, M. P. The Theil-Sen Estimator with Doubly Censored Data and Applications to Astronomy. *J. Am. Stat. Assoc.* **90**, 170-177 (1995).
94. Kendall, M. G. *Rank correlation methods, 2nd ed.* (Hafner Publishing Co., 1955).
95. Livezey, R. E. & Chen, W. Y. Statistical field significance and its determination by Monte Carlo techniques. *Mon. Wea. Rev.* **111**, 46-59 (1983).

Figures

ECMWF Precip Fcst vs CMAP: 1992–2008

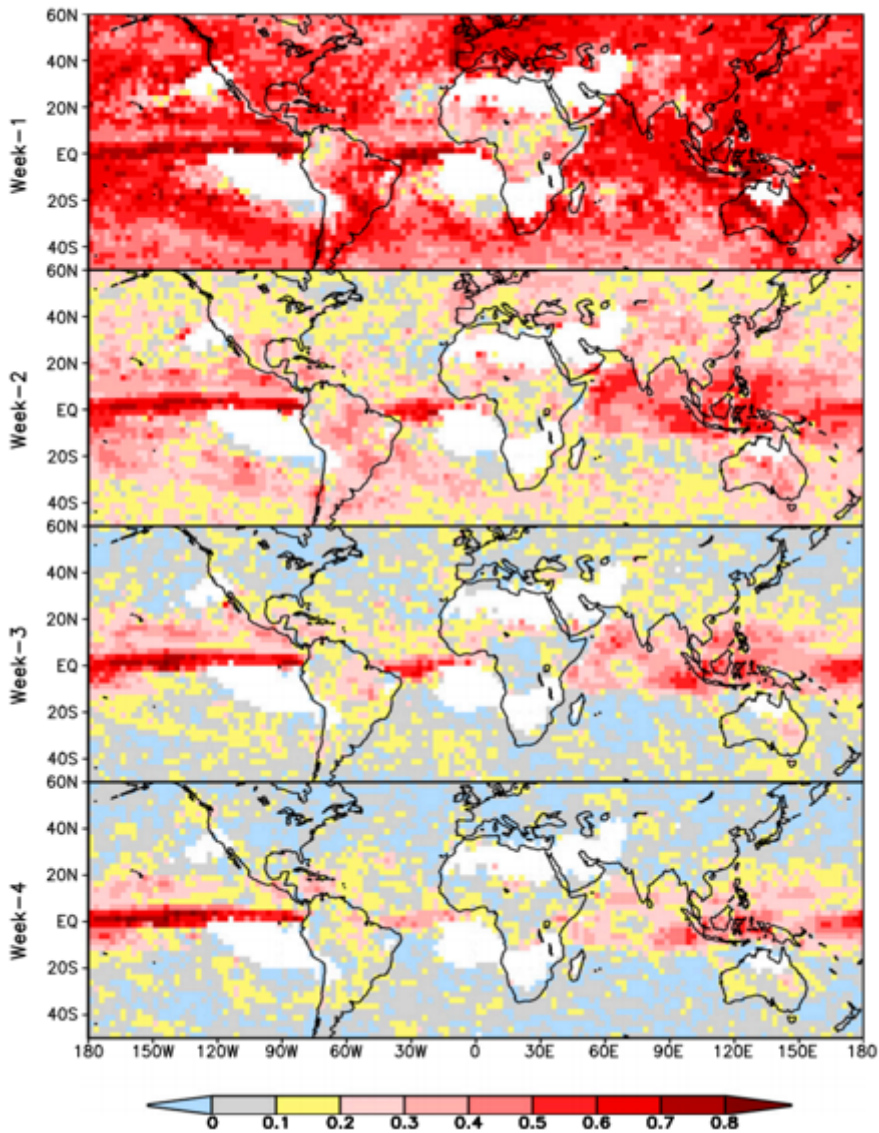


Figure 1

Subseasonal prediction skill of precipitation by ECMWF. Shown is the correlation between ECMWF precipitation hindcast and CMAP rainfall data for Weeks 1-4 during 1992-2008. The white area denotes dry mask during June-September, where the total CMAP rainfall over 122 days is less than 20 mm. [Adopted from Li and Robertson (2015).]

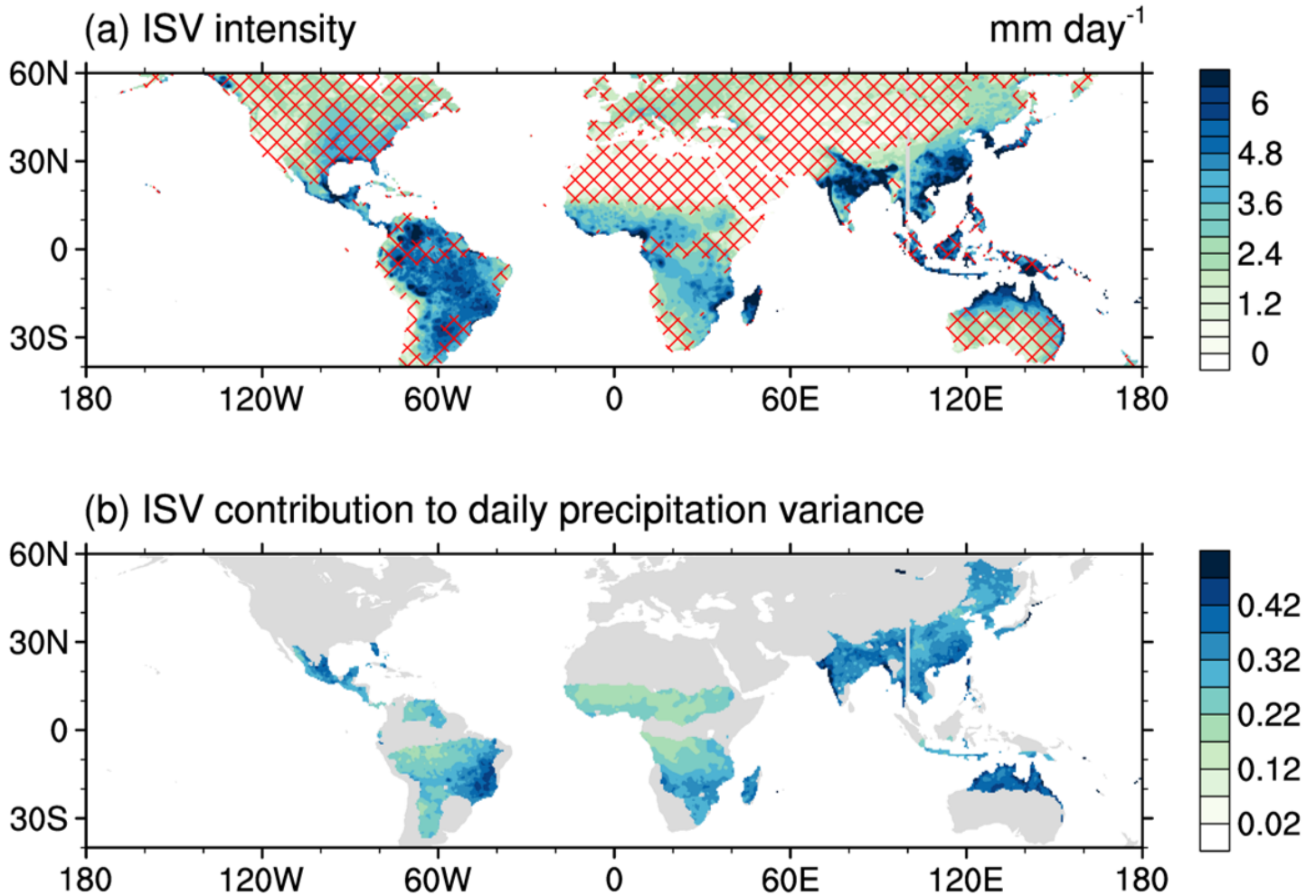


Figure 2

Climatological ISV activity in monsoon seasons during 1979-2018. a is summer (MJJAS for NH and NDJFM for SH) ISV intensity (mm day⁻¹) defined by the standard deviation of 8-70-day bandpass-filtered precipitation anomalies. Cross-hatching marks the region outside the global land monsoon. A monsoon region is defined by the local summer-minus-winter precipitation exceeding 300 mm, and the summer precipitation exceeding 55% of the annual total (Wang and Ding 2008). b shows the 8-70-day ISV variance contribution to the total daily precipitation variance. The contribution is calculated by the ratio of the averaged power spectrum in the intraseasonal band to the total power. The area-conserving format is used in which the variance is proportional to the area of the logarithm of frequency versus power times frequency.

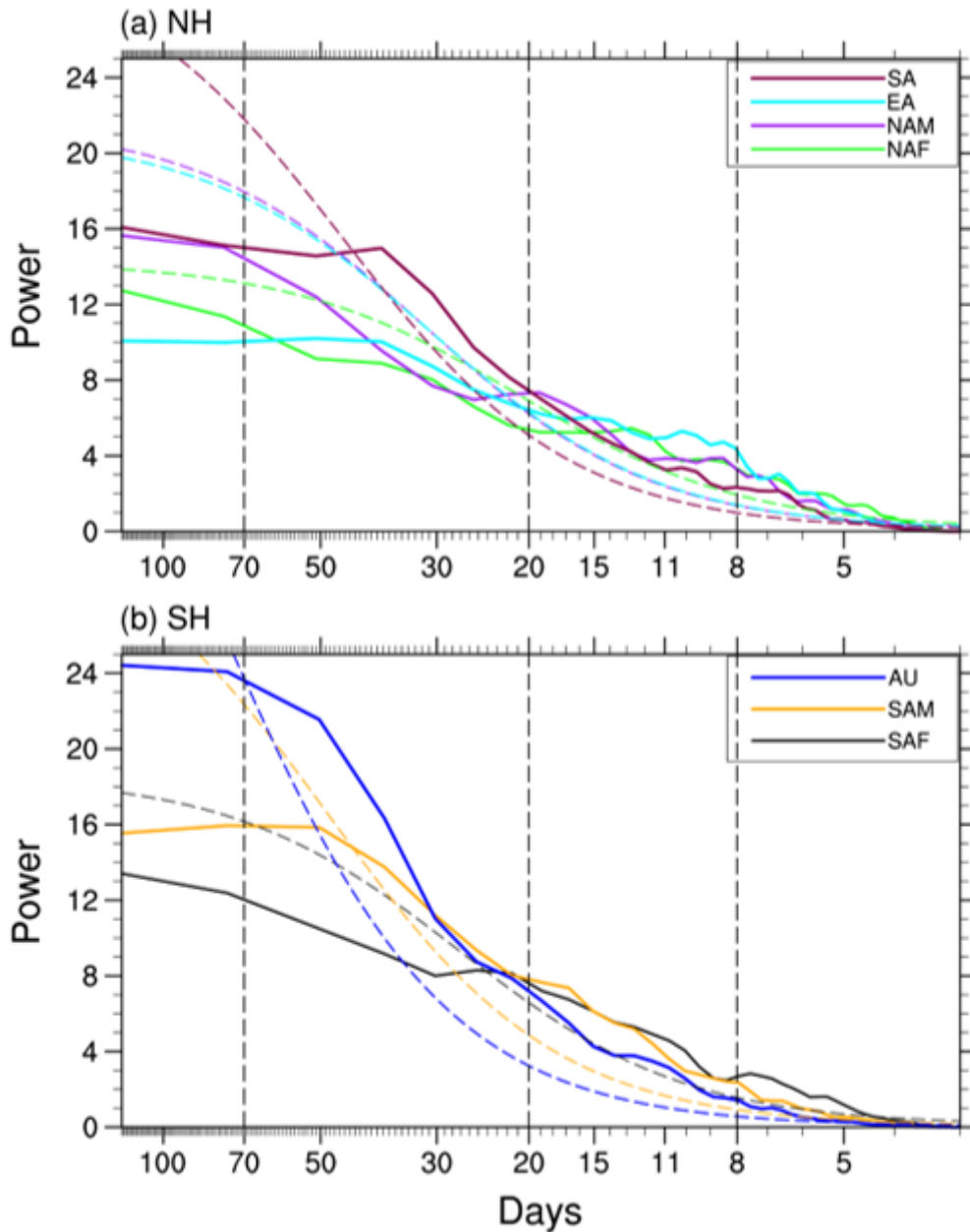


Figure 3

Power spectra of ISVs of individual monsoons. Power spectra of the 3-day running mean precipitation anomalies (mm day⁻¹) averaged over each monsoon region for the summers of 1979-2018. Daily climatology is removed to obtain the anomalies. Each monsoon precipitation series is normalized before the spectrum analysis. Dashed lines denote the corresponding 90% confidence levels.

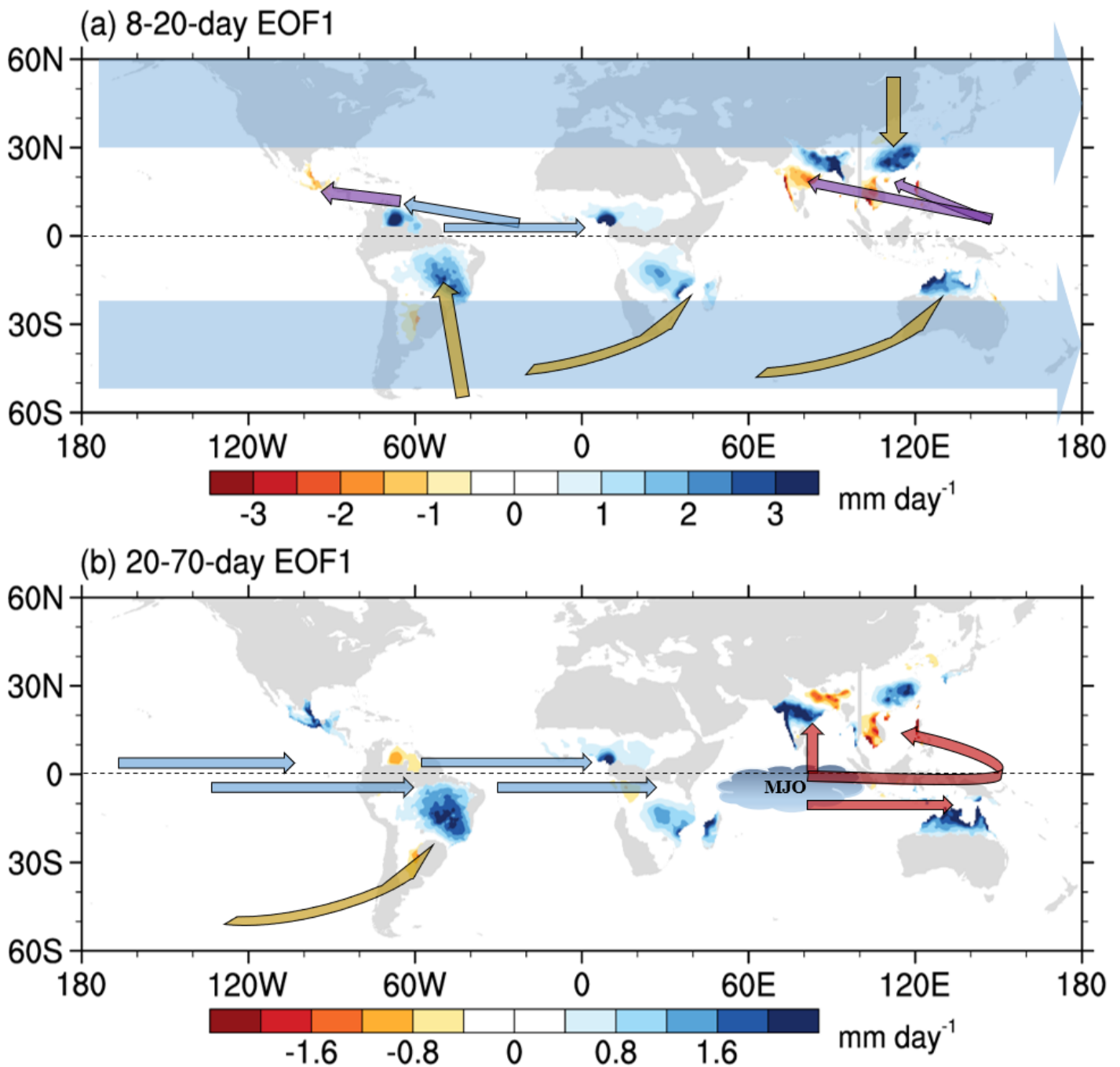


Figure 4

Dominant ISV modes in individual land monsoon regions and their propagation tracks for 8-20-day and 20-70-day components. The spatial patterns of the first EOF modes of summer ISV precipitation anomalies (shading; mm day⁻¹) over each monsoon region from 1979-2018. The arrows show the propagation routes before the wet peak phase of ISV events in each region. The purple and red arrows illustrate the preceding signals from quasi-biweekly oscillation in a and MJO convection in b, respectively. The eastward and westward blue arrows indicate the preceding wave propagation tracks associated with the equatorial Kelvin and mixed Rossby-gravity waves. The brown arrows indicate teleconnection forcing

from the extratropics. The broad light-blue arrows in a denote the background westerly zone where mid-latitude wave trains prevail. The propagation tracks are schematics based on the lead-lag regressed maps onto leading ISV modes.

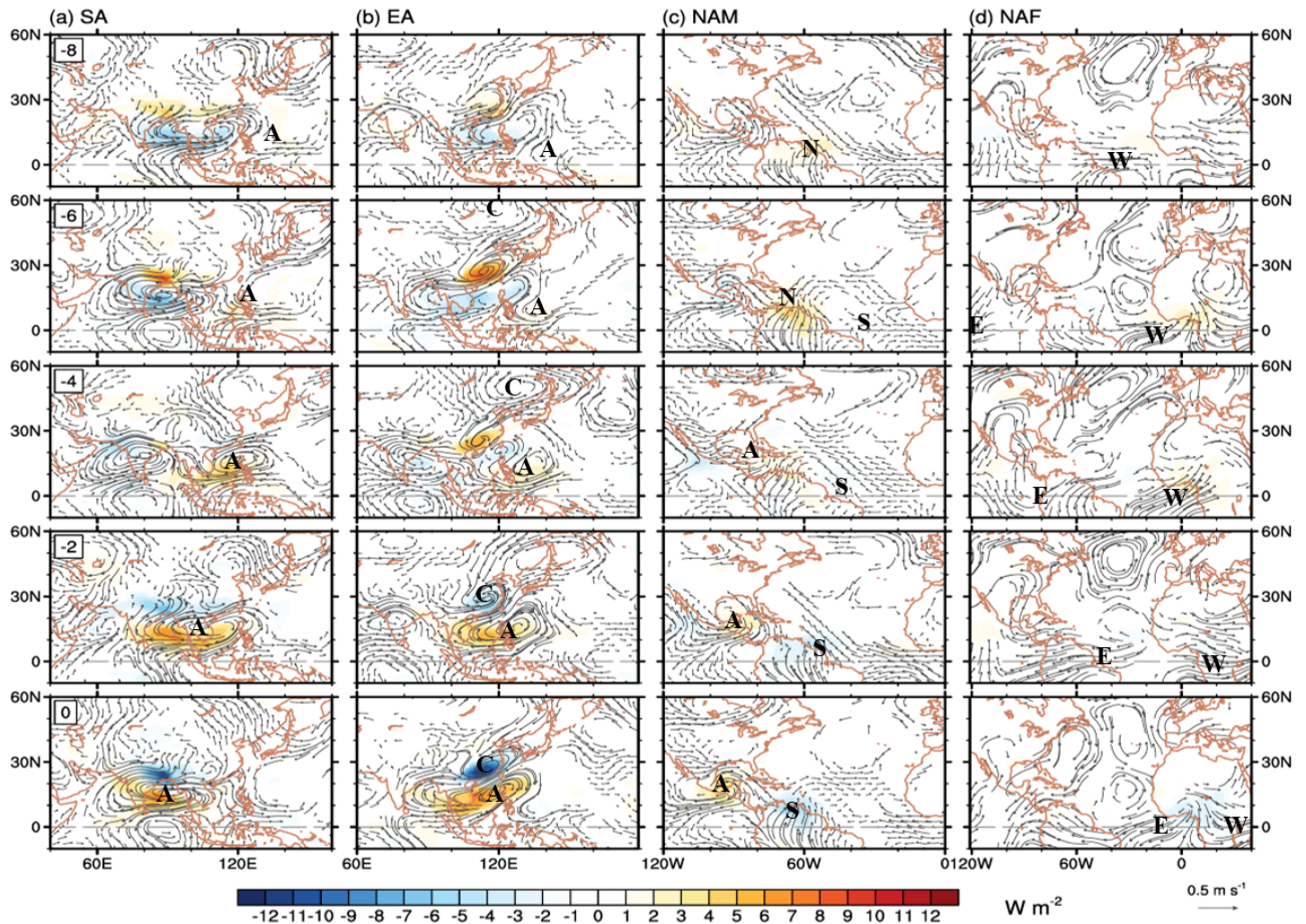


Figure 5

Origin and propagation of 8-20-day ISVs in NH summer monsoon regions. Shown are the lead-lag regressed maps of 8-20-day filtered OLR (shading; $W m^{-2}$) and wind (vector, $m s^{-1}$) anomalies onto the PC1s during the summers of 1979-2018 for a South Asian (SA), b East Asian (EA), c North American (NAM), and d northern African (NAF) monsoons. The wind anomalies shown in a, b, and c are at 850 hPa, while those in d are at 200 hPa. Only OLR and wind anomalies significant at the 90% confidence level are shown. Letter A tracks the center of the anomalous anticyclone; C, the cyclone; S, the southerly; N, the northerly; E, the easterly; and W, the westerly.

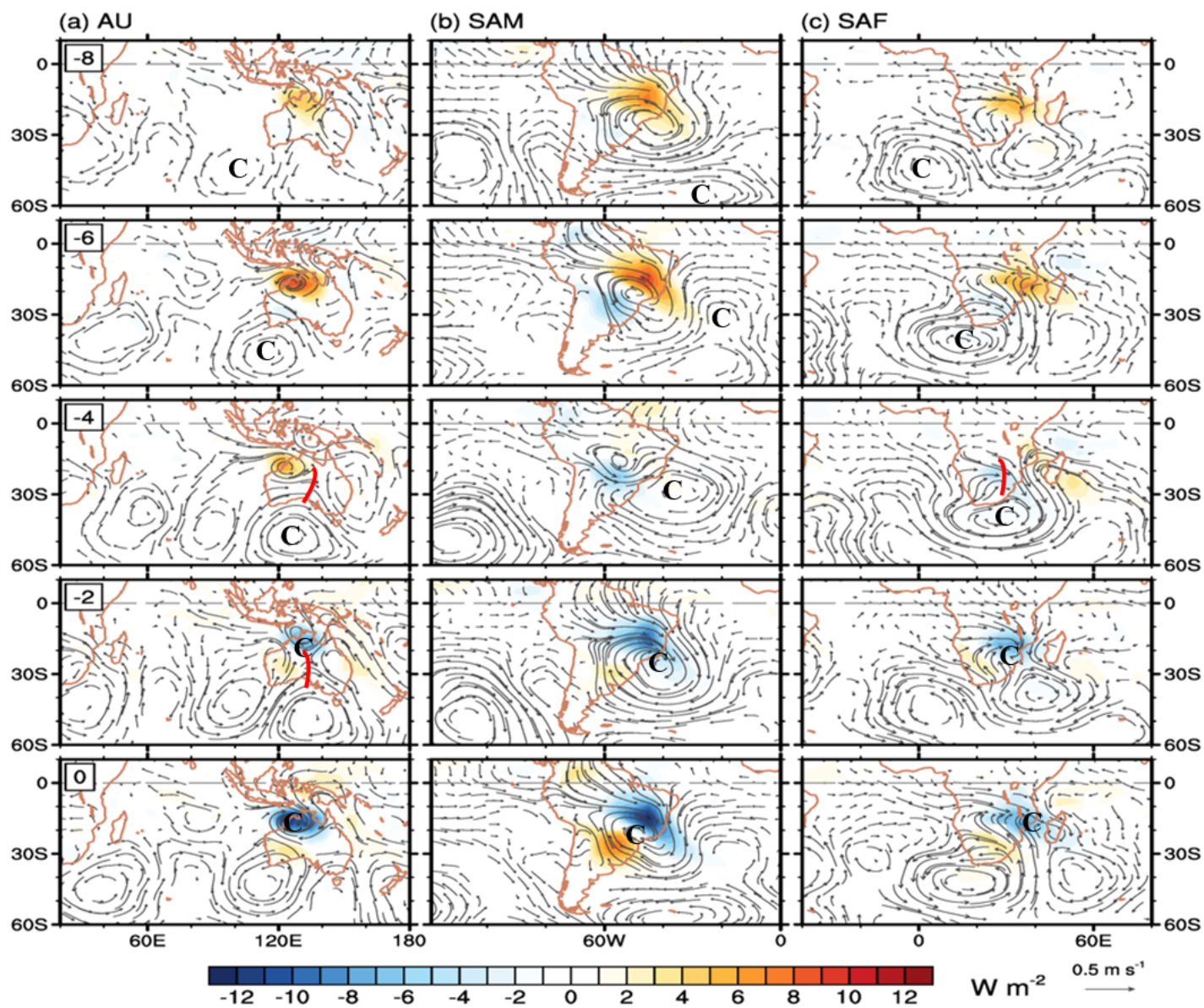


Figure 6

Origins of 8-20-day ISVs of SH summer monsoons. Same as Fig. 5, except for 850-hPa wind anomalies in SH: a Australian (AU), b South American (SAM), and c South African (SAF) monsoons. The redline denotes the trough center at 850 hPa.

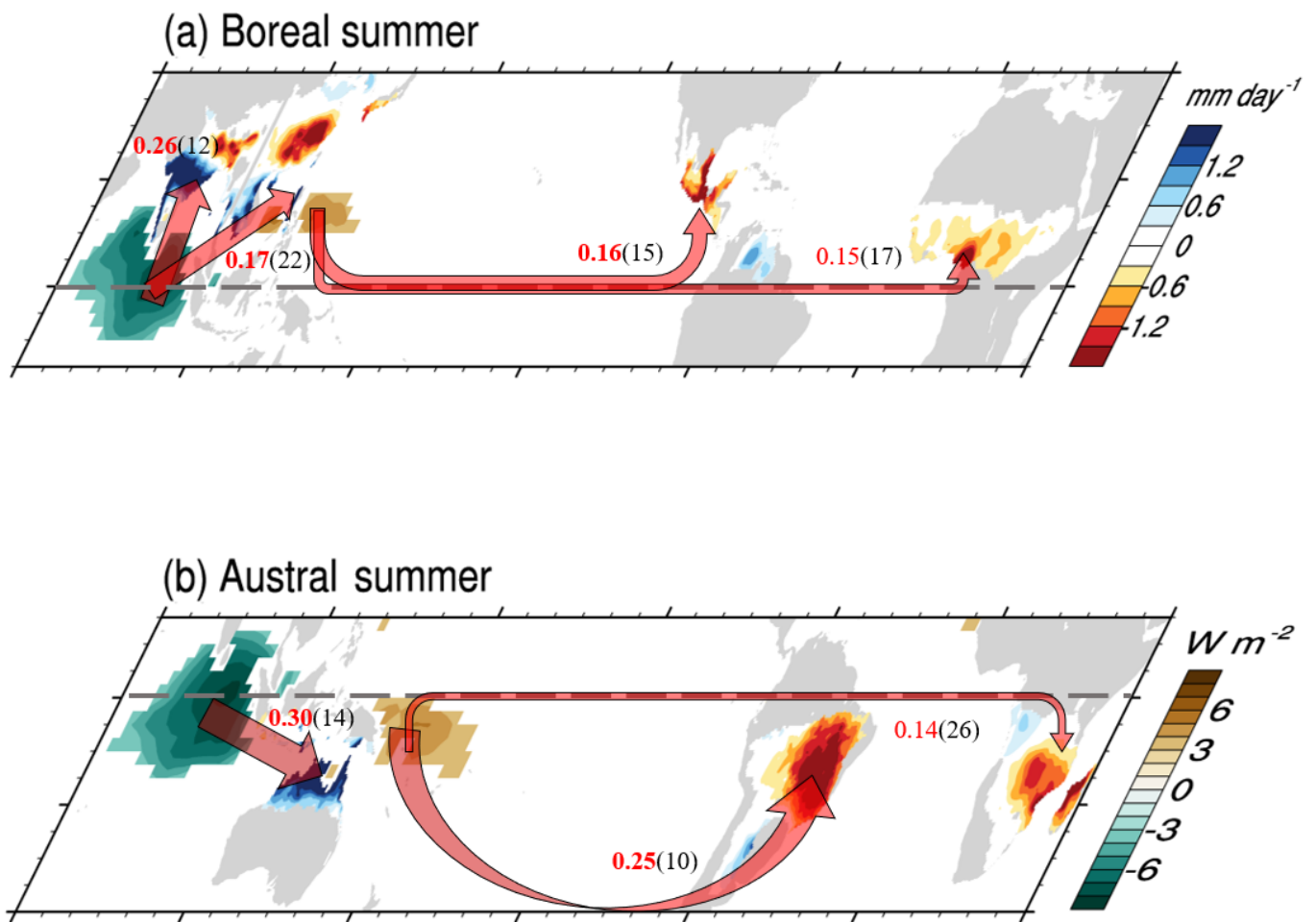


Figure 7

Role of MJO in modulating 20-70-day ISVs in individual summer monsoon regions. Red Arrows indicate lead correlations between MJO convective center in equatorial central Indian Ocean (or associated negative convective anomaly in tropical western Pacific) and the leading modes of 20-70-day ISVs over individual monsoon regions. Shading over ocean and land denotes the regressed OLR anomaly ($W m^{-2}$) onto the negative RMM2 and the leading EOF pattern ($mm day^{-1}$) of each monsoon shown in Fig. 4b, respectively. The sign of the EOF in Fig. 4b is reversed when the maximum correlation coefficient is negative. The values in red indicate the maximum correlation coefficient, and the values in the bracket show the leading days, respectively. All correlations are significant at the 90% confidence level, except for the two African monsoons.

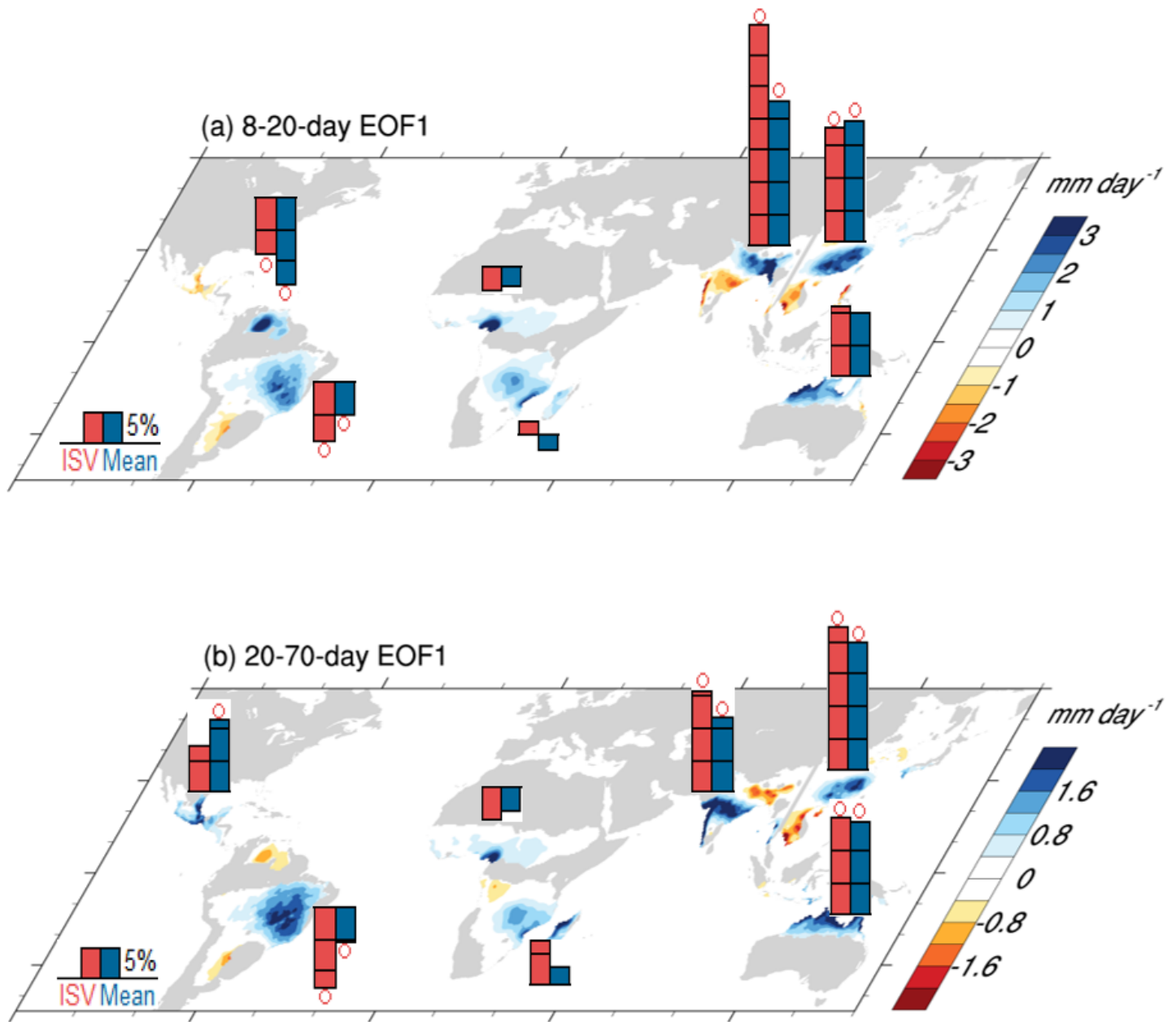


Figure 8

Trends in the ISV intensity of individual summer monsoons during 1979-2018. The red bars show the trends (units in percentage change) of the ISV amplitude averaged over the wet regions of the leading EOF (same shading as in Fig. 4) anomalies above 0.05 mm day^{-1} for a 8-20-day and b 20-70-day ISVs. The blue bars show the corresponding trends in the area-averaged seasonal-mean precipitation. The ISV amplitude is defined by the local-summer standard deviation of filtered precipitation anomaly. Significant trends at the 90% confidence level based on the Mann-Kendall rank statistics are marked by red circles.

Supplementary Files

This is a list of supplementary files associated with this preprint. [Click to download.](#)

- [Supplementary.docx](#)